International Journal of Nanomedicine

Dovepress
open access to scientific and medical research

Open Access Full Text Article

ORIGINAL RESEARCH

S-Doped Hollow Multi-Metallic Prussian Blue Analogue (PBA) Nanoplatform for Enhanced Anticancer for Cervical Cancer

Lu Xu[1,*], Jing Liu[2,*], Suli Li[1], Xingchen Lu[1], Wenjie Gu[1], Shunhua Zhu[1], Meng Wang[1], Xiaojin Wu[3], Qingli Huang[1]

[1]Public Experimental Research Center of Xuzhou Medical University, Xuzhou, Jiangsu Province, 221004, People's Republic of China; [2]Department of Neurology, the Affiliated Xuzhou Municipal Hospital of Xuzhou Medical University, Xuzhou No. 1 People's Hospital, Xuzhou, Jiangsu Province, 221100, People's Republic of China; [3]Department of radiotherapy, the affiliated Xuzhou Municipal Hospital of Xuzhou Medical University, Xuzhou No. 1 People's Hospital, Xuzhou, Jiangsu Province, 221100, People's Republic of China

*These authors contributed equally to this work

Correspondence: Xiaojin Wu; Qingli Huang, Email xiaojinwu@xzhmu.edu.cn; qlhuang@xzhmu.edu.cn

Purpose: Developing novel multimodal nanomaterials-based anticancer agents to meet complex clinical demands is an urgent challenge. This study presents a novel uniform hollow S-doped NiCuFe Prussian blue analogue (NiCuFe-S) with satisfactory size and properties as anticancer agents for efficient cervical cancer therapy using a simple and environmentally friendly procedure.

Methods: The formation mechanism and the reason for enhanced performance of NiCuFe-S were characterized and discussed by diverse spectroscopic and microscopic methods. Moreover, to demonstrate the anti-cancer ability of NiCuFe-S, in vitro and in vivo experiments were carried out.

Results: Compared to the non-doped NiCuFe, the NiCuFe-S exhibited significantly enhanced photothermal and catalytic activity attributed to the electronic bandgap-narrowing effect and the increased electron circuit paths resulting from S doping. The hollow structure of NiCuFe-S facilitated the loading of small-molecule drugs, such as doxorubicin (DOX), transforming it into a multimodal nanoplatform for cervical cancer treatment. In vitro and in vivo experiments proved the potential of the NiCuFe-S nanotheranostic agent for chemodynamic therapy (CDT), photothermal therapy (PTT), and chemotherapy for cervical cancer.

Conclusion: This research not only overcomes inherent limitations but also significantly broadens the applications of Prussian blue analogues in biomedicine.

Keywords: nanomaterials, Prussian blue analogue, catalytic, photothermal therapy, anticancer

Introduction

With the development of nanotechnology, various nanomaterials-based cancer therapy strategies including photothermal therapy (PTT), chemodynamic therapy (CDT) and other novel methods were developed and have arisen as research hotspots for researchers, emphasizing the importance of nanoparticles endowed with photothermal or catalytic properties in achieving successful treatment outcomes.[1–10] PTT is a novel noninvasive cancer treatment, which can switch light energy into hyperthermia at tumor site by employing site-specific nanoparticles with photothermal conversion performance.[1,3,4,11,12] In this way, PTT could induce apoptosis and/or necrosis of cancer cells and achieve ideal curative effect. CDT is defined as an in-situ treatment with little side effects, which could kill cancer cells effectively by highly toxic hydroxyl radical (·OH) using metal-related to Fenton reaction or Fenton-like reaction in mildly acidic conditions of cancer.[2,5,6,13–16] And, many studies have proved the synergistic anti-tumor effect of PTT combined with CDT, which achieved superior outcomes than the single mode of PTT and CDT.[17–20] This combination therapy not only could synchronously kill cancer cells by hyperthermia of PTT and reactive oxygen species (ROS) of CDT to enhance the efficiency of cancer therapy but also enhance the production of ROS by PTT during the period of therapy.[17–20]

Received: 25 June 2024
Accepted: 20 August 2024
Published: 24 August 2024

Various nanostructures, including noble metal nanomaterials, inorganic nanoparticles, polymer nanocomposites, and organic nanostructures, have been successfully designed and fabricated to enhance photothermal or catalytic properties, thereby improving the efficiency of cancer treatment.[1–20] Among them, traditional transition metal-based nanomaterials including metals oxides, metals sulfides and metals hydroxides of Ni, Cu, Fe, Mn have attracted numerous attentions for anticancer due to their outstanding photothermal or catalytic properties, and facile preparation.[21–23] However, poor biocompatibility and small specific surface area of traditional nanomaterials often limited their further application. Fortunately, when integrated them into a metal-organic frameworks (MOFs) with desired size (<100nm), it will possess large surface area, porosity, and good biocompatibility, which is expected as a potential candidate for application for cancer therapy.[24–29] Metal-organic frameworks (MOFs), with their unique framework featuring high porosity, large specific surface area, and adjustable metal nodes or organic ligands, have garnered substantial attention for their versatility in energy, biomedicine, catalysis, and other applications.[24–29] As a subclass of MOFs, Prussian blue analogues (PBAs) have elicited substantial interest and explored as platforms for diagnosis and treatment for various diseases due to lower cost, simpler synthesis, and more adjustable catalytic activity.[27–35] However, there are limited reports on the cancer therapy application of PBAs, primarily due to their poor NIR absorption and low photothermal conversion efficiency. Enhancing the photothermal efficiency of PBAs and developing PBA-based anticancer agents for efficient treatment for cancer is significant to meet complex clinical demands. Heteroatom doping has been proposed as a viable approach to enhance the inherent properties of nanomaterials by regulating their electronic structure.[36–40] For instance, Zhu et al reported enhanced interfacial electron transfer and improved catalytic activity in ($g\text{-}C_3N_4$)/MS_2 (M=Sn, Zr) heterojunctions through O, S doping.[39] The difference in charge density indicated that interfacial electron transfer was increased by O and S doping, thus further improving the catalytic activity of nanocomposites. Su et al developed a sulfur (S)-doped ($Ti{-}S{-}TiO_2{-}x$) nanocomposite with outstanding photothermal conversion efficiency, attributing it to the introduction of oxygen deficiency by S dopants, which improved NIR absorption and the efficiency of electron–hole separation.[40]

Herein, we prepared a novel uniform hollow S-doped NiCuFe Prussian blue analogue (NiCuFe-S) with satisfactory size (<100nm) and properties as anticancer agents for cervical cancer using a simple and environmentally friendly procedure. As illustrated in Scheme 1, hollow S-doped NiCuFe PBAs were synthesized using a facile method. Our study revealed superior photothermal conversion performance and catalytic activity in S-doped PBAs compared to non-doped PBAs, a topic that has been largely understudied. Additionally, the formation mechanism of NiCuFe-S PBAs and the reason on their enhanced performance were comprehensively investigated. Vitro and vivo experiments proved that the prepared hollow S-doped NiCuFe PBAs could serve as a novel nanoplatform for enhanced photothermal and ROS anticancer therapy against cervical cancer. This research proved the feasibility of tumor therapy using S-doped PBA as anticancer agents and significantly expanded the potential of their applications in biomedicine.

Experimental Section

Materials, Characterization and Performance

All chemicals and characterization instruments were all listed in supplementary materials (S1 and S2). The photothermal and catalytic performance of hollow NiCuFe-S were evaluated using NIR laser irradiation and 3,3′,5,5′-tetramethylbenzidine (TMB) following early procedures (S3).

Synthesis of NiCuFe-S

Initially, NiCuFe-PBA nanocubes were synthesized following a modified procedure[41] (S4). Subsequently, 10 mL of 2.8 mg/mL sodium sulfide aqueous solution was added to the 20 mL NiCuFe-PBA ethanol suspensions (0.5 mg/mL) with stirring. The mixed solution was then placed into an autoclave and maintained at 100°C for 6 h. The resulting hollow S-doped NiCuFe PBA was obtained through centrifugation and washing, denoted as NiCuFe-S. To enhance biocompatibility and enable chemotherapy, small-molecule PEG and chemotherapy drug DOX were modified and loaded onto NiCuFe-S, resulting in P-NiCuFe-S and DP-NiCuFe-S, respectively. Typically, PEG was added to 20 mL of deionized water at a mass ratio of 1:1 with NiCuFe-S and stirred at room temperature for 6 h. After the precipitate was collected by centrifugation and then added to tris solution with the same mass of DOX and stirred for 6 h. The precipitates were collected by centrifugation.

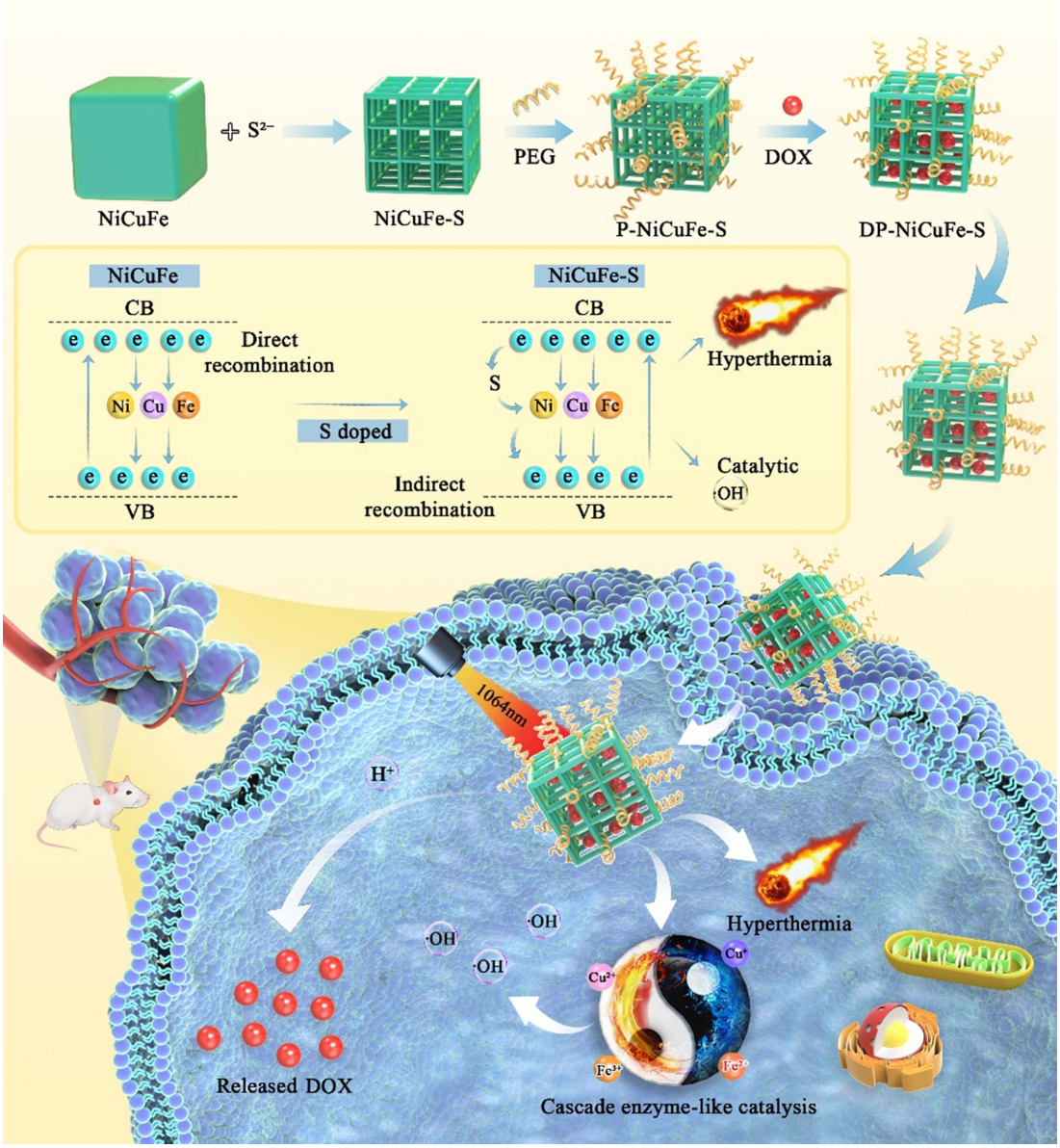

Scheme 1 The illustration of construction of S doped hollow multi-metallic NiCuFe-S nanoplatform and its application for enhanced anticancer for cervical cancer.

In vitro Anti-Cancer Experiments of Hollow NiCuFe-S

Initially, the biocompatibility and biosafety of the prepared hollow NiCuFe-S were evaluated in vitro using the normal cell line (NRK-52E) with the traditional Cell Counting Kit (CCK8) method. Subsequently, human cervical cancer Hela cells were co-incubated with the hollow NiCuFe-S nanoplatform to investigate the in vitro anti-cancer performance of NiCuFe-S, employing the CCK8 assay. All cells were purchased from the Procell Life Science & Technology Co (Wuhan, China). More details were shown in S5.

To visually confirm the anti-cancer effect of NiCuFe-S, Calcein AM (green fluorescence)/propidium iodide (PI, red fluorescence) live/dead stain experiments were conducted. Hela cells (1×10^4 cells) were seeded into 96-well plates and incubated in an incubator for 12 hours. After treated with P-NiCuFe-S and DP-NiCuFe-S of 100 μg/mL in different groups for another 4 hours, Calcein-AM/PI (KeyGen) solution (100 μL) for staining live/dead cells was used to replace the supernatant in 96 well plate. The experiments were observed with different colors under the inverted fluorescence microscope (Olympus IX73). Intracellular reactive oxygen species (ROS) assay, flow cytometry assay, and Western blot experiments were also performed to confirm the anti-cancer performance of NiCuFe-S nanoplatform in vitro. The details were shown in S6.

In vivo Anti-Cancer Performance of Hollow NiCuFe-S

All experimental protocols involving animals were carried out with permission from the Institutional Animal Care and Use Committee (IACUC) of Xuzhou Medical University (permission NO.202309T022 in 2023), and the procedures were as per the regulations and guidelines of IACUC (Guidelines for ethical review of experimental animal welfare in Xuzhou Medical University). The animal tumor models were established using balb/c nude female mice (6 weeks old, GemPharmatech LLC, Jiangsu, China) by injecting Hela cells (6×10^5). Once tumors reached a certain size (approximately 100 mm^3), mice were injected through the tail vein on days 2 and 10 with modified and drug-loaded NiCuFe-S (P-NiCuFe-S and DP-NiCuFe-S). Mice were divided into six groups (n = 5 per group) based on different treatment programs: control (injected with PBS), control+NIR (injected with PBS and laser irradiation (1064 nm, 1.0 W/cm^{-2}, 5 minutes)), P-NiCuFe-S (injected with modified NiCuFe-S), P-NiCuFe-S+NIR (injected with modified NiCuFe-S and laser irradiation (1064 nm, 1.0 W/cm^{-2}, 5 minutes)), DP-NiCuFe-S (injected with drug-loaded NiCuFe-S), and DP-NiCuFe-S+NIR (injected with drug-loaded NiCuFe-S and laser irradiation (1064 nm, 1.0 W/cm^{-2}, 5 minutes)). During the process of laser irradiation, real-time temperature changes at the tumor site were monitored using an infrared thermal imager, and infrared thermal imaging images of the tumor site were recorded at 1, 2, 3, 4, and 5 minutes. The weights and tumor sizes of mice were monitored every two days for 16 days, and weight change curves and volume changes for each group were plotted according to experimental records. Finally, the mice were euthanized after 16 days, and the tumor tissue and main organs were harvested for H&E staining. Additionally, analyses for blood routine parameters and blood biochemistry were performed using blood samples taken through the retroorbital plexus region of mice in each group after anti-cancer treatment. The blood samples were left at room temperature for 2 h and centrifuged at 4°C with 3000 rpm for 15 min, and then the supernatant was taken for biochemical detection. The blood samples extracting in vacutainer (containing 3.2% sodium citrate anticoagulant) were taken 200 μL for the blood routine parameters.

Results and Discussion

Characterization

Transmission electron microscopy (TEM) and scanning electron microscopy (SEM) were utilized to examine the morphological evolution of the prepared samples. As depicted in Figure 1a, uniform NiCuFe nanocubes with an average size of approximately 50 nm were obtained through a modified precipitation method. Subsequently, these nanocubes were subjected to treatment with Na_2S, resulting in the formation of hollow S-doped NiCuFe, as illustrated in Figure 1b. SEM images (Figure 1c) revealed the presence of holes, providing further confirmation of the hollow structure after hydrothermal treatment with Na_2S. Energy dispersive X-ray (EDX) spectrum analysis was performed to investigate the elemental compositions of hollow S-doped NiCuFe in Figure 1d. The presence of six elements, namely C, N, S, Ni, Fe, and Cu, was confirmed, validating successful S doping. These elements were found to be homogeneously distributed in all hollow cubes, as indicated by EDX mapping images (Figure 1e–k), validating the uniform distribution of S dopants. X-ray diffraction (XRD) was employed to examine variations in the crystal structure (Figure 1l). Typical peaks at 17.3, 24.6, 35.1, and 39.4° were observed, consistent with the early report on NiCuFe.[41] Importantly, after doping with S^{2-}, no substantial change was found in the XRD pattern, indicating that the addition of S^{2-} did not affect the crystal structure. X-ray photoelectron spectroscopy (XPS) experiments also prove this result. In Figure 1m and n, we can find that low valence of Fe^{2+} and Cu^{+} become dominant valence state in NiCuFe-S after S doping, which will enhance the Fenton-like catalytic activity of the PBAs.

Performance Testing

We found strong UV–vis absorption of NiCuFe from 600 nm to 1100 nm after S doping in Figure S1, which will benefit to its photothermal performance. In Figure 2, the photothermal properties of NiCuFe-S were investigated. The photothermal-induced temperatures of NiCuFe-S were significantly higher than those of NiCuFe and water, as depicted in Figure 2a and b. The temperature of the NiCuFe-S aqueous suspension rose rapidly to 45.7 °C in 5 min under 808 nm laser radiation (1.5 W/cm^2), resulting in an approximately 18.7 °C temperature increase. In contrast, only temperature increases of 1.2°C and 2.1°C were observed in water and NiCuFe aqueous suspension under the same conditions (Figure 2a and b). Moreover, an apparent concentration-dependent and laser power-dependent photothermal effect was

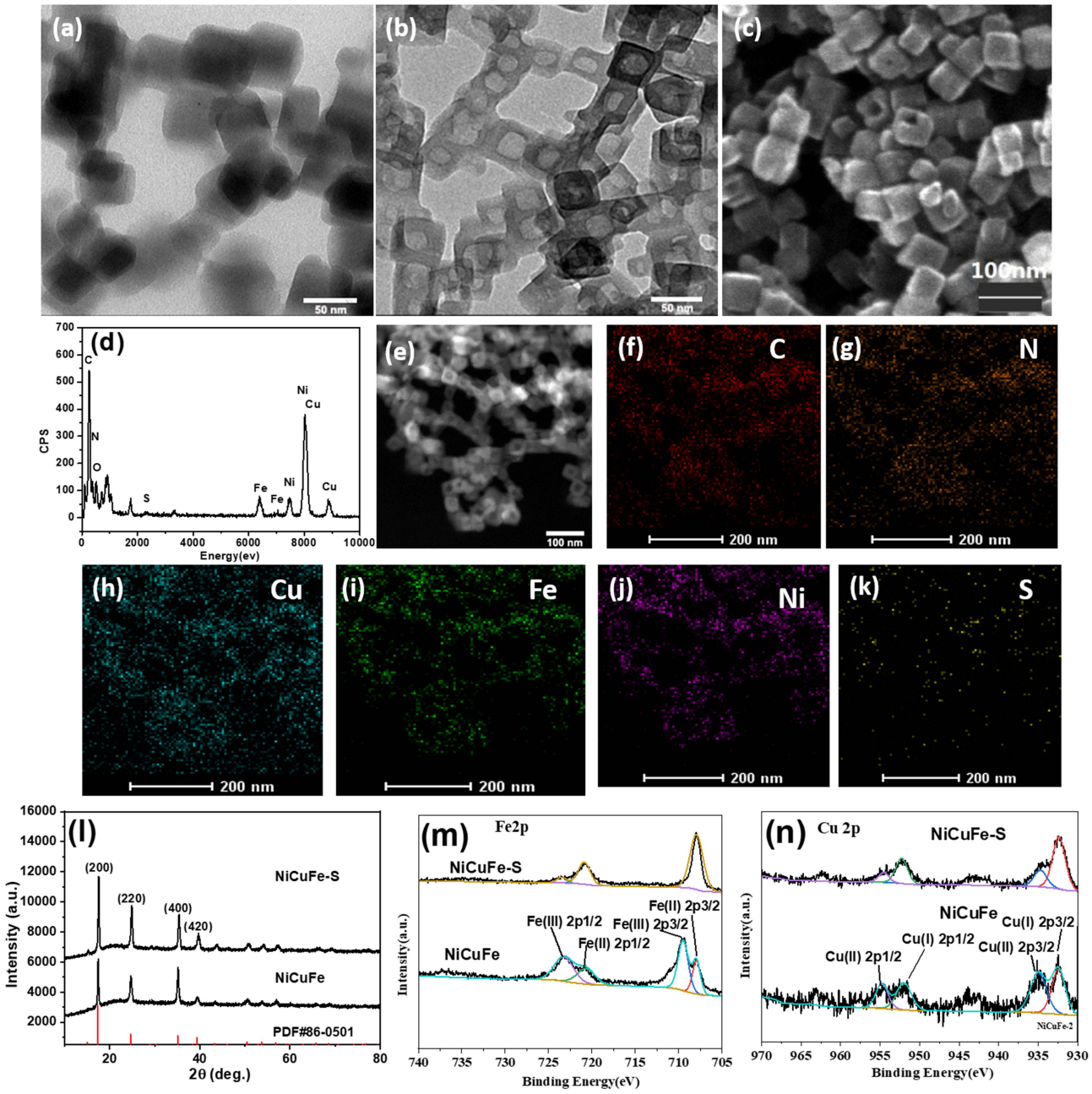

Figure 1 TEM images of (**a**) NiCuFe (**b**) NiCuFe-S (**c**) the SEM images of NiCuFe-S (**d**) EDS spectrum and (**e**) the HAADF images and (**f–k**) EDS mapping NiCuFe-S (**l**) XRD (**m** and **n**) XPS spectra of Fe 2p and Cu 2p in NiCuFe and NiCuFe-S.

observed (Figure 2c and Figure S2). When the concentration of NiCuFe-S aqueous suspension increased to 500 μg/mL, a 33.3°C temperature change was observed, indicative of a typical state of hyperthermia. As Figure 2d shows, photothermal stability experiments were conducted by monitoring the temperature variation every 30 minutes during laser on/off irradiation, repeated five times. The maximum temperature of each cycle remained almost identical, demonstrating the good photo and thermal stability of the hollow NiCuFe-S. The photothermal conversion efficiency was also calculated according to early methods in Figure 2e and 2f which is approximately 52.1% and superior than many other PB-based nanomaterials reported in previous literatures.[42–45] According to earlier reports highlighting the desirable deeper tissue penetration ability of the second NIR (NIR-II) light compared to the first NIR (NIR-I) laser,[46,47] the photothermal performance of NiCuFe-S in the second NIR (NIR-II) bio-windows (1064 nm) was also evaluated. The

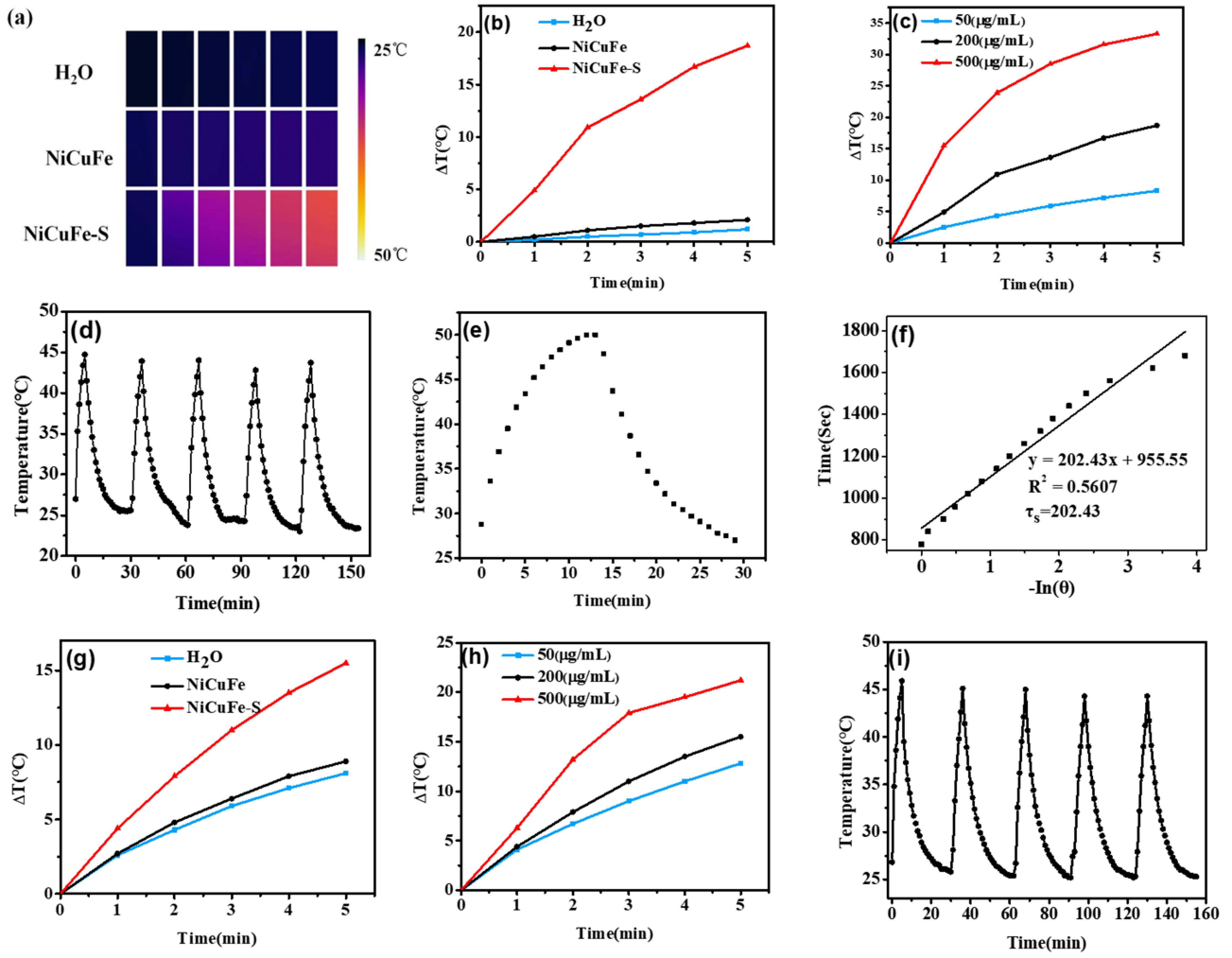

Figure 2 (**a**) Thermal infrared images of H_2O and the as-prepared nanomaterials (NiCuFe and NiCuFe-S) solutions (200 μg/mL) under 808 nm NIR laser irradiation (1.5 W/cm^2) for 5 min and (**b**) the corresponding heating curves (**c**) heating curves of NiCuFe-S solutions with different concentrations (**d**) The photothermal stability of NiCuFe-S dispersion (200 μg/mL) by five cycles of laser on/off irradiation under 808 nm laser irradiation (1.5 W/cm^2) (**e**) The course of the temperature of the NiCuFe-S dispersion (200 μg/mL) under 808 nm laser irradiation (1.5 W/cm^2) to the highest point, followed by cooling to room temperature after turning off the laser, respectively (**f**) The linear relationship of time data versus −ln θ obtained from the cooling period of picture under 808 nm respectively (**g**) Heating curves of H_2O and the as-prepared nanomaterials (NiCuFe and NiCuFe-S) solutions (200 μg/mL) under 1064 nm NIR laser irradiation (1.0 W/cm^2) for 5 min (**h**) the corresponding heating curves (**i**) The photothermal stability of NiCuFe-S dispersion (200 μg/mL) by five cycles of laser on/off irradiation under 1064 nm laser irradiation (1.0W/cm^2).

same trend was observed, as depicted in Figure 2g–i. All experimental results indicated that NiCuFe-S has the valuable potential to enhance photothermal therapy in both NIR-I and NIR-II dual windows.

PBAs exhibit outstanding catalytic activity due to the presence of adjustable metal active sites, crucial for enhancing catalytic performance. As shown in Figure 3, peroxidase-like activity was investigated using TMB as an indicator. Compared to H_2O_2 and NiCuFe, the as-prepared hollow NiCuFe-S showed the highest UV–vis absorption peaks at 652 nm and 895 nm in Figure 3a, suggesting higher catalytic performance than H_2O_2 and NiCuFe. Furthermore, acidic conditions were found to be more suitable for enzyme-like catalytic reactions than a neutral environment (Figure 3b), aligning with the acidic nature of the tumor microenvironment, making it more conducive to target cancer. Additionally, even at a reduced concentration of 1 μg/mL, significant peaks were observed (Figure 3c), indicating the high efficiency of the catalytic performance of NiCuFe-S. The typical Michaelis–Menten model was used to investigate the apparent steady-state kinetic parameters (Km). The Km values were 0.838 mM by changing the concentration of TMB in Figure 3d and e, comparable to Fe-Ag_2S (0.821 mM) and MoS_2@$MgFe_2O_4$ (0.806 mM) nanozymes in earlier literature.[48,49] These results indicate that the as-prepared hollow NiCuFe-S exhibited excellent peroxidase-like activity. ESR spectroscopy with DMPO as a spin-trapping agent was also conducted (Figure 3f). Higher ESR signals were detected in NiCuFe-S than in H_2O_2 and NiCuFe, indicating the generation of more ·OH by NiCuFe-S.

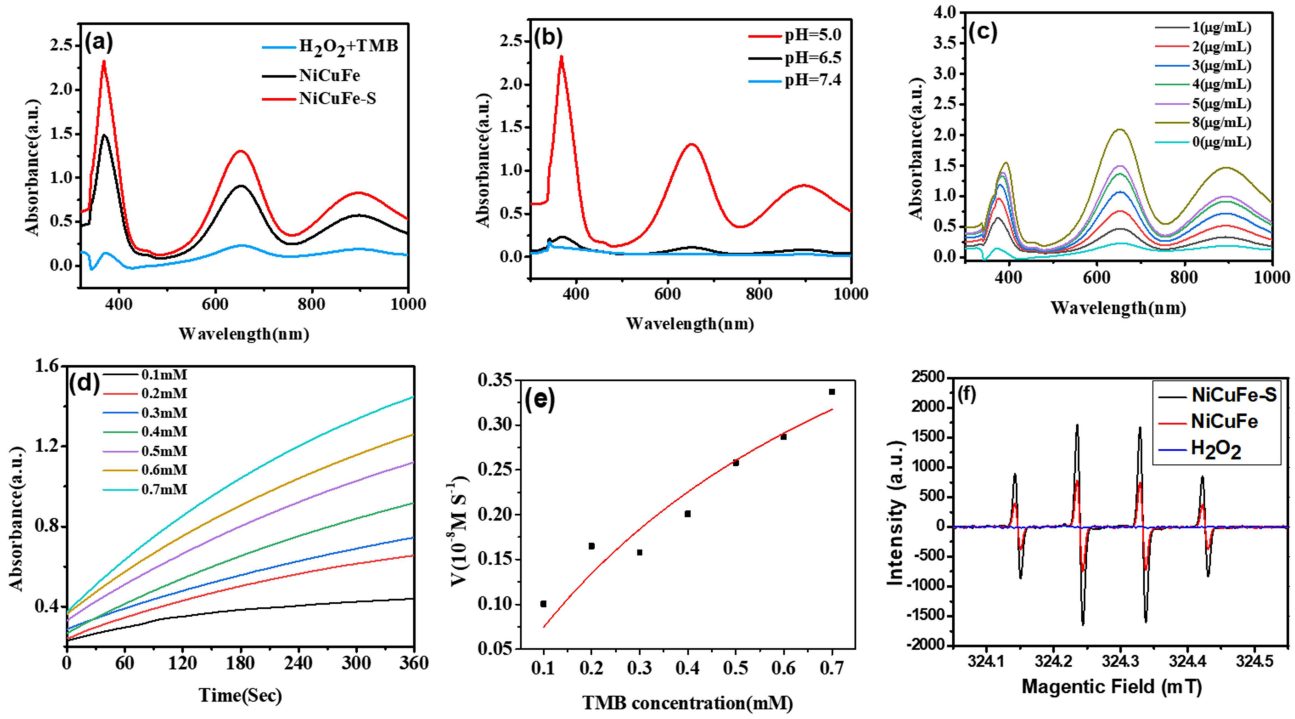

Figure 3 (**a**) Enzyme catalytic activity of the as-prepared nanomaterials (NiCuFe and NiCuFe-S) on TMB at pH 5.0 (nanomaterials, 16 μg/mL; TMB 0.1M; H_2O_2, 50 mM; pH 5.0) (**b**) Enzyme catalytic activity of NiCuFe-S on TMB at different pH (**c**) Enzyme catalytic activity of NiCuFe-S with different concentrations. (**d**) Kinetic study of NiCuFe-S against different concentration of TMB (**e**) The Michaelis–Menten curves of NiCuFe-S against the mentioned concentration of TMB (**f**) EPR spectra of H_2O_2, NiCuFe and NiCuFe-S.

Mechanism Analysis

The mechanisms of the formation of the hollow structures and their outstanding performances were comprehensively investigated. The formation of hollow structures can be ascribed to the differential diffusion rates between metal ions and S^{2-} ions. In this case, when the Na_2S solution was added to the solid NiCuFe nanocubes, outward transport of metal ions and inward transport of S^{2-} ions occurred. However, as a result of the larger size of S^{2-} ions, they diffused more slowly than metal ions, leading to the reactions predominantly occurring in the outer layers. As a result, the valence states of some metal ions (Fe^{3+} and Cu^{2+}) were adjusted, leading to the formation of a hollow structure with high photothermal and catalytic performance, as illustrated in Scheme 1.[50] The semiconductor's band structure is crucial for its efficiency and optical properties. The band gaps of NiCuFe-S (Eg values) were calculated and found to be 1.85 eV and 1.83 eV for NiCuFe and NiCuFe-S in Figure S3, respectively. The doping of heteroatoms (S atom) into the PBA lattice induced a net electronic bandgap-narrowing effect, resulting in red-shifting and moving closer to the NIR regime due to the lower bandgap energy. Moreover, the introduction of heteroatoms (S atom) increased the electron circuit paths, reducing the recombination of electron–hole pairs and promoting the catalytic activity of PBAs.

Therapeutic Properties of NiCuFe-S in vitro

Considering the outstanding photothermal and catalytic properties discussed earlier, the S-doped PBA was anticipated to replace Prussian blue as a new platform with higher performance for tumor therapy. The construction of the nanoplatform of hollow NiCuFe-S and their anti-cancer properties in vitro is demonstrated in Figure 4. Initially, biocompatible polyethylene glycol (PEG) was surface-modified on the NiCuFe-S to enhance their biosafety, a critical factor for the clinical application of nanotherapeutics.

FTIR analysis in Figure S4 revealed the successful PEG coating due to new peaks of C-O at 989 cm^{-1}.[51] Subsequently, the PBAs loaded with the cytotoxic chemotherapy drug, DOX, leveraging the porous and high specific surface properties of MOFs. Figure 4a and Figure S5 also demonstrated the presence of PEG and DOX, as evidenced by

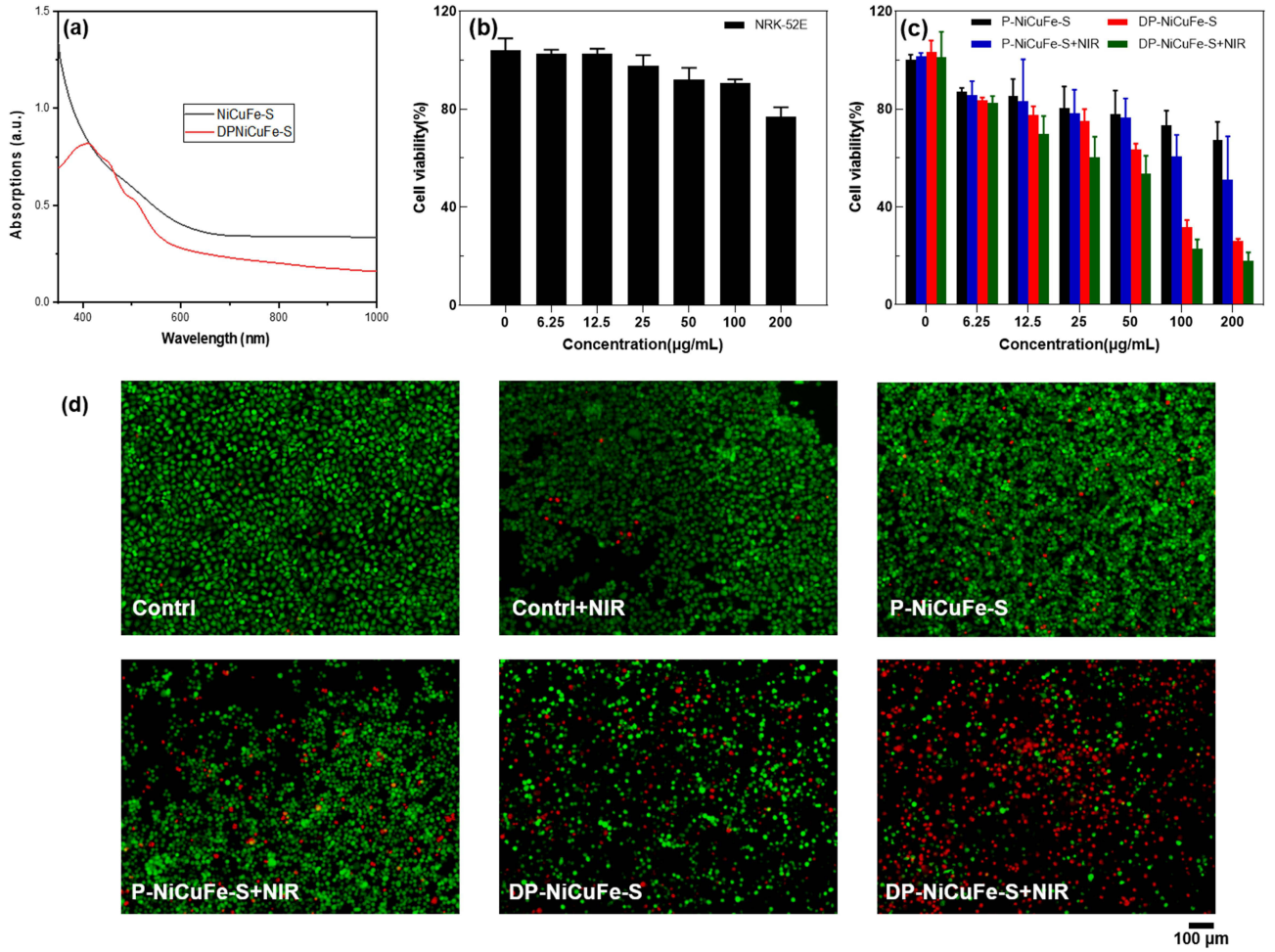

Figure 4 (**a**) Absorption spectra of NiCuFe-S and DP-NiCuFe-S (**b**) Cell viability of normal NRK-52E cells treated with P-NiCuFe-S at different concentrations (n=3). (**c**) Cell viability of Hela cells treated with P-NiCuFe-S, P-NiCuFe-S+NIR, DP-NiCuFe-S, DP-NiCuFe-S-NIR for 24h, respectively ("+NIR" means with 1064 nm, 1.0W/cm^2, 5min laser irradiation) (n=3). (**d**) Fluorescence images of calcein-AM/PI double-staining Hela cells after incubation with PBS, PBS+NIR, P-NiCuFe-S, P-NiCuFe-S+NIR, DP-NiCuFe-S, DP-NiCuFe-S+NIR, respectively.

the appearance of DOX absorption at 480 nm and the significant change in Zeta potential. Furthermore, we also found that the modification of PEG and loading DOX had little affection of the morphologies and properties of NiCuFe-S in Figures S6 and S7. The DOX loading rate was also calculated, which is about 96.0%, as per the following formula, which is higher than early reports on similar nanostructures:[35,36] Drug Load rate = (loaded DOX/input DOX)*100%.

As shown in Figure 4b, more than 80% of normal NRK-52E cells survived, even as the concentrations of PEG-modified NiCuFe-S increased to 200 μg/mL. This survival rate was superior to that of most PBAs reported in earlier studies.[35,52] Subsequently, human cervical cancer Hela cells were selected to investigate the anticancer performance of the prepared nanoplatform (P-NiCuFe-S and DP-NiCuFe-S) in vitro (Figure 4c). Six experimental groups with different treatments were established: I: PBS (pH 7.4, 10 mM); II: PBS+1064 nm laser irradiation (1.0 W/cm^2, 5 min); III: P-NiCuFe-S (0, 6.25, 12.5, 25, 50, 100, 200μg/mL); IV: P-NiCuFe-S (0, 6.25, 12.5, 25, 50, 100, 200μg/mL) +1064 nm laser irradiation (1.0 W/cm^2, 5 min); V: DP-NiCuFe-S (0, 6.25, 12.5, 25, 50, 100, 200μg/mL); VI: DP-NiCuFe-S (0, 6.25, 12.5, 25, 50, 100, 200μg/mL) +1064 nm laser irradiation (1.0 W/cm^2, 5 min). Observations revealed that almost no cells were killed in groups I and II. Group III (P-NiCuFe-S only) exhibited a slight killing effect on Hela cells at high concentrations (50, 100, 200 μg/mL), attributed to the outstanding catalytic activity in the acidic environment of cancer cells. In comparison, DP-NiCuFe-S in group V caused some harm to the cells, with 31.9% and 26.0% of cells killed at concentrations of 100 and 200 μg/mL, respectively. Importantly, the released DOX played a significant role in inhibiting tumor cells through chemotherapy effects, as shown in Figure S8. Similarly, cells in group IV showed approximately

50% mortality, while 50% of cancer cells died when treated with P-NiCuFe-S and laser irradiation. Excitingly, the survival rate dropped to less than 20% for Hela cells in group VI when treated with the constructed nanoplatform (DP-NiCuFe-S, 200 μg/mL) under 1064 nm laser irradiation for 5 min attributed to the synergistic effect of multi-mode treatments. Fluorescence microscope images of cells in different groups stained by AM and PI assay were acquired to distinguish between living and dead cells (Figure 4d). The highest cell mortality was observed in group VI, followed by group V, group IV, group III, group II and group I, consistent with the CCK 8 assay results. These findings further confirm the in vitro advanced therapeutic effect of hollow S-doped NiCuFe PBAs.

Mechanism of Anti-Tumor of NiCuFe-S

Understanding the mechanisms underlying the anti-tumor properties of nanomaterials is crucial for their medical application in cancer treatment. In this context, various experiments were conducted to explore the subcellular localization of hollow cubes, intracellular ROS production, and marker protein levels in Hela cells. As shown in Figure 5a and b, typical images of cells treated with DP-NiCuFe-S revealed the presence of many hollow nanocubes in the cytoplasm, confirming efficient uptake by cancer cells. Once taken up, these hollow PBA nanocubes were triggered by the acidic tumor microenvironment (TME), characterized by excessive H^+, H_2O_2, and GSH. On the one hand, the peroxidase-like performance of NiCuFe-S was activated by the abundant H^+ and H_2O_2 in TME. This led to the generation of large amounts of reactive oxygen species (ROS) through a cascade of Fenton-like reactions involving transition metal ions (Cu^{2+}/Cu^+ and Fe^{3+}/Fe^{2+}), as demonstrated in the intracellular ROS production experiments in Figure 5c. The use of DCFH-DA as a probe converted it into dichlorofluorescein (DCF) with green fluorescence under oxidative stress in cells. The fluorescence signals observed in the cells treated with the nanocubes confirmed ROS production and NIR irradiation enhanced the signals, indicating nanocube degradation and increased •OH generation, leading to enhanced cell apoptosis. On the other hand, as the nanocubes degraded in the TME,

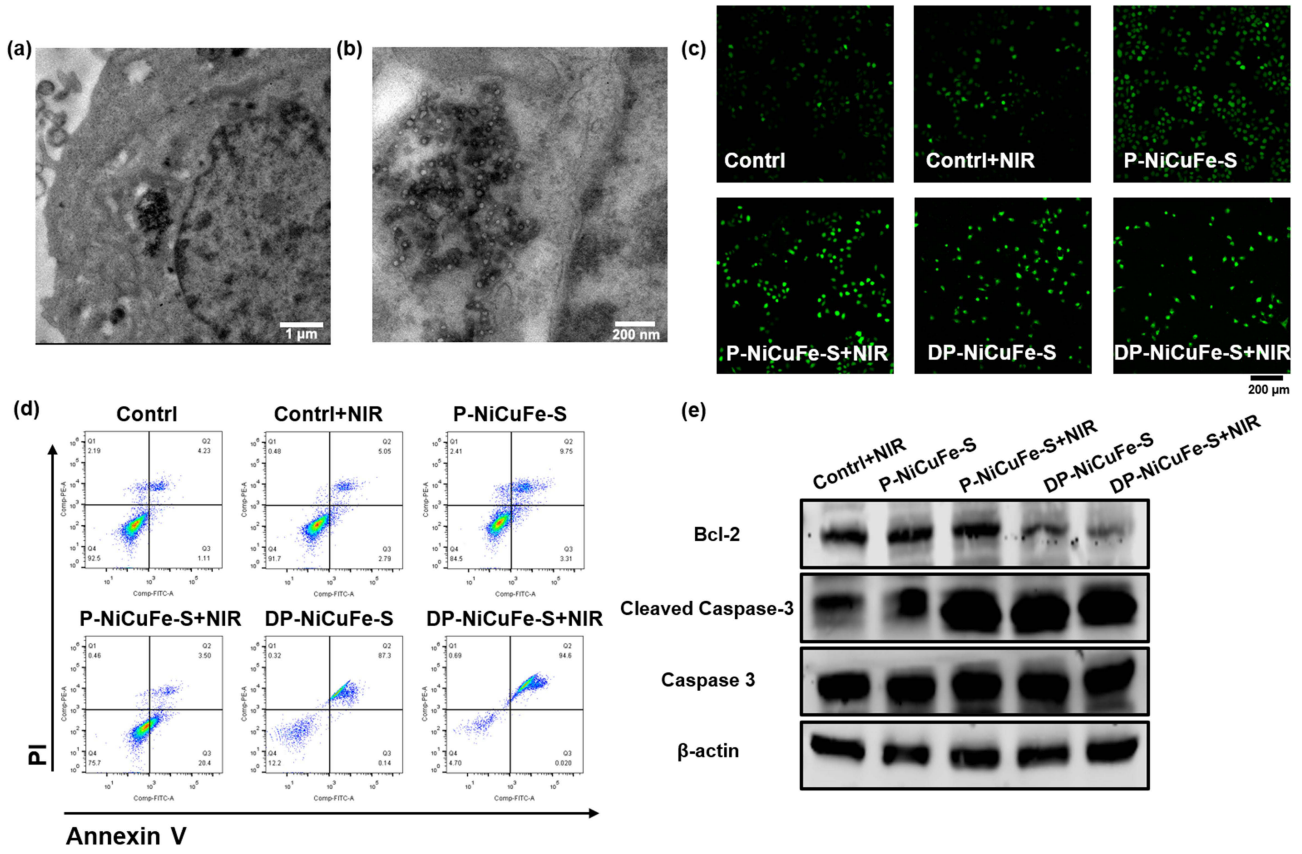

Figure 5 (**a** and **b**) TEM images of Hela cells after treatment with DP-NiCuFe-S. (**c**) Intracellular DCF fluorescence of Hela cells after incubation with PBS, PBS+NIR, P-NiCuFe-S, P-NiCuFe-S+NIR, DP-NiCuFe-S, DP-NiCuFe-S+NIR. (**d**) Flow cytometry analysis of cell apoptosis in Hela cells treated with different formulations. (**e**) Western blot of the protein expression of Bcl-2, caspase-3, cleaved-caspase-3 in Hela cells from different treatments.

DOX was sustainably released in the hollow section, triggering targeted chemotherapy for cancer and reducing the side effects of traditional chemotherapy. Furthermore, the prepared NiCuFe-S exhibited excellent photothermal conversion performance. The introduction of NIR laser irradiation achieved local hyperthermia at the tumor site, further enhancing ROS production and DOX release. To further elucidate the antitumor mechanism of NiCuFe-S, flow cytometry was employed to quantitatively detect apoptosis through Annexin V-FITC/PI double staining. In Figure 5d, Hela cells treated with irradiation alone showed negligible necrotic and apoptotic cells. Compared to NiCuFe-S, the percentage of apoptotic cells in NiCuFe-S treated with laser irradiation (NiCuFe-S+NIR) and DP-NiCuFe-S increased to 23.90 % and 87.44%, respectively. The DP-NiCuFe-S+NIR group exhibited the highest apoptosis rate (94.62%). Further investigation into the molecular-level impact of NiCuFe-S on the apoptosis pathway revealed a significant decrease in the expression of antiapoptotic protein Bcl-2 and a notable increase in cleaved caspase-3 levels in DP-NiCuFe-S groups in Figure 5e, suggesting that DP-NiCuFe induced tumor cell apoptosis to the greatest extent. Moreover, the photothermal effect enhanced the antitumor efficacy of these nanomaterials in vitro.

Therapeutic Properties of NiCuFe-S in vivo

The in vivo antitumor experiments of the NiCuFe-S nanoplatform were conducted using balb/c nude female mice, as depicted in Figure 6. The tumor model was established by injecting Hela cells, and all mice underwent the treatment procedure outlined in Figure 6a. According to the treatment methods, the mice were divided into six groups (5 mice per

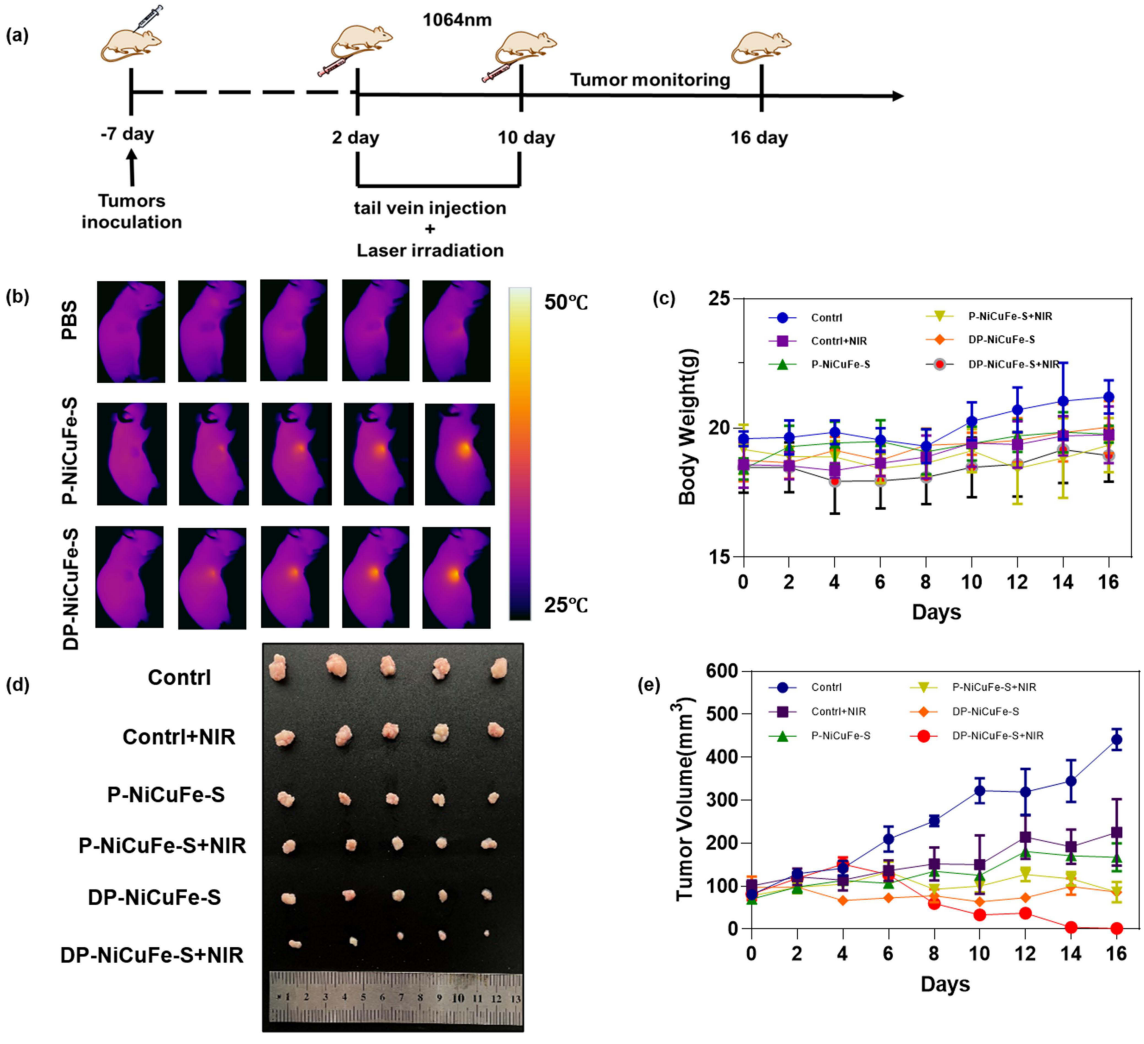

Figure 6 (**a**) Schematic illustration of therapeutic protocol for tumor-bearing mice (**b**) Typical thermal images of tumor-bearing mice under NIR irradiation after tail injection of P-NiCuFe-S and DP-NiCuFe-S (**c**) Animal body weight change curves. (**d**) Images of tumors of tumor-bearing mouse after 16 days treated with different formulations (PBS, PBS+NIR, P-NiCuFe-S, P-NiCuFe-S+NIR, DP-NiCuFe-S, and DP-NiCuFe-S+NIR). (**e**) The corresponding curves of the relative volume of tumors from different treatment.

group): I: intravenous injection of PBS (pH 7.4, 10 mM); II: intravenous injection of PBS+1064 nm laser irradiation; III: intravenous injection of P-NiCuFe-S (5 mg/kg); IV: intravenous injection of P-NiCuFe-S (5 mg/kg)+1064 nm laser irradiation (1.0 W cm^{-2}, 5 min); V: intravenous injection of DP-NiCuFe-S (5 mg/kg); VI: intravenous injection of DP-NiCuFe-S (5 mg/kg)+1064 nm laser irradiation (1.0 W cm^{-2}, 5 min). First, photothermal images in the laser irradiation groups (groups II, IV, and VI) were obtained to evaluate the antitumor efficacy of NiCuFe-S in vivo (Figure 6b). In comparison to the negligible temperature fluctuation of tumors in the PBS + 1064 nm laser irradiation group (II group), the temperature at the tumor sites in groups IV and VI (intravenous injection of P-NiCuFe-S (5 mg/kg) + 1064 nm laser irradiation and intravenous injection of DP-NiCuFe-S (5 mg/kg) + 1064 nm laser irradiation group) increased rapidly, demonstrating the satisfactory photothermal performance of NiCuFe-S in vivo. Next, the tumor sizes and mice weights in the different groups were recorded (Figure 6c–e). No significant change in the body weight of all mice was observed (Figure 6c), indicating negligible side effects of the nanoplatforms on normal organs. However, for tumors, despite achieving a certain

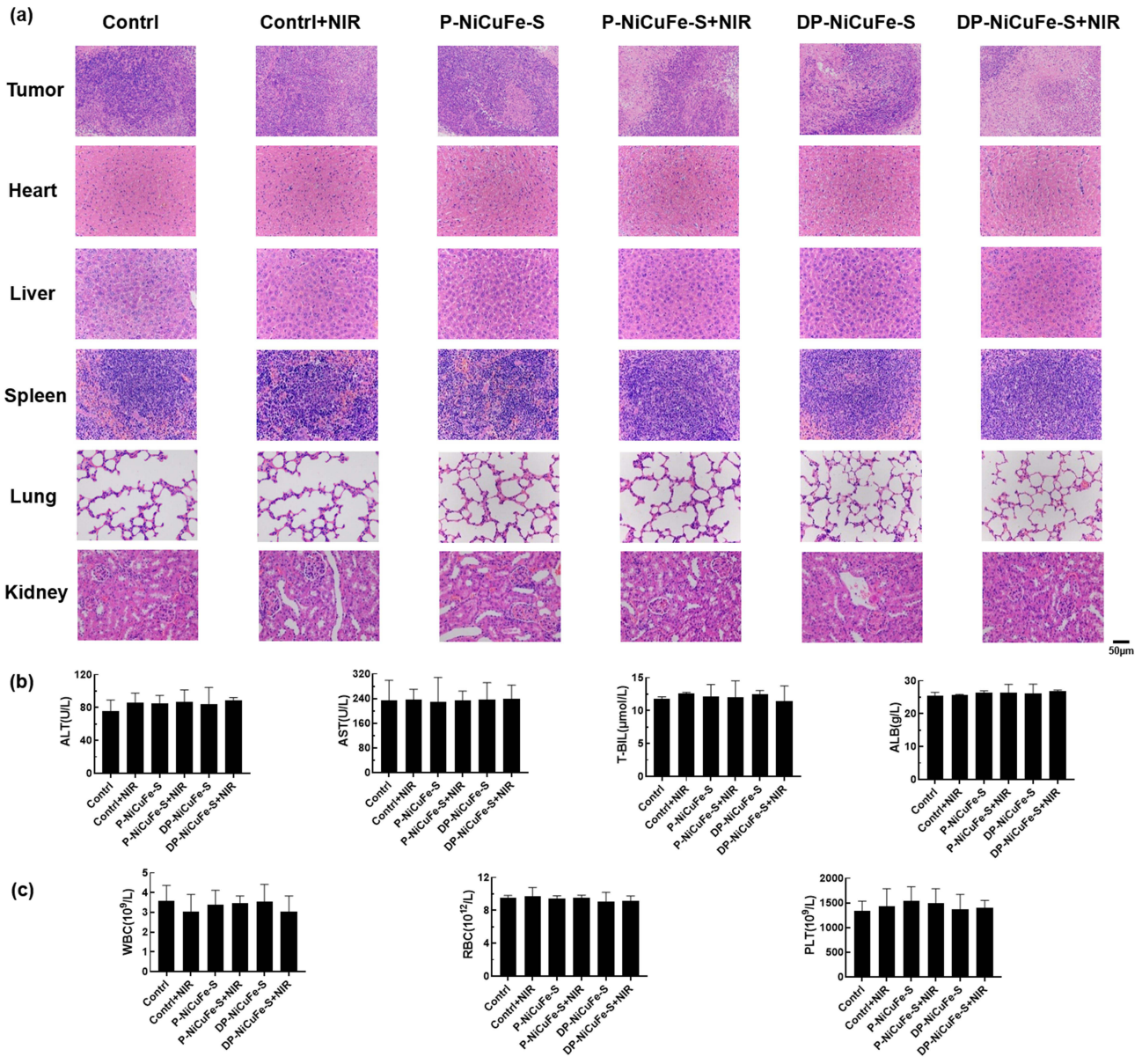

Figure 7 (**a**) H&E-stained sections of the tumor tissue and main organs from Hela tumor-bearing mice in various groups, Scale bar, 100 μm. (**b** and **c**) Typical biochemical parameters for Hela tumor-bearing mice in various groups (notes: ALT-alanine aminotransferase; AST: aspartate aminotransferase; T-BIL-total bilirubin; ALB-albumin; WBC-white blood cells; RBC-red blood cells; PLT- platelet).

therapeutic effect in groups III, IV, and V, the VI group (intravenous injection of P-NiCuFe-S (5 mg/kg) + 1064 nm laser irradiation) displayed the best tumor inhibition efficacy among all groups (Figure 6d and e), indicating the synergistic effect of PTT, chemodynamic therapy (CDT), and chemotherapy in the treatment process. To further investigate the biosafety profile of the NiCuFe-S nanoplatform, major organs (heart, liver, spleen, lung, and kidney) and tumors of the mice were harvested after 16 days of treatment, and hematoxylin and eosin (H&E) staining experiments were performed (Figure 7a). Negligible tissue damage or inflammatory lesions were observed, indicating little toxicity of NiCuFe-S in vivo. However, at tumor site, the nucleus of tumor cells was large and were pale blue in control group. For the P-NiCuFe-S+NIR group treated tumors, the cancer cells were clearly damaged and got local necrosis, indicating that the nanomaterials had superior killing ability against tumor. Additionally, no significant differences were detected in the listed blood routine indexes and blood biochemistry parameters (Figure 7b and c), confirming the good biocompatibility of the as-prepared NiCuFe-S. These results collectively demonstrate the good biosafety profile and high anti-cancer efficiency of the developed NiCuFe-S nanoplatform.

Conclusion

Overall, this work successfully constructed a novel anti-cancer nanoplatform based on uniform hollow S-doped NiCuFe PBA. The introduction of S dopants significantly enhanced the photothermal conversion efficiency and enzyme-like catalytic activity of PBAs. In vitro and in vivo experiments confirmed the excellent anti-cancer performance of the S-doped PBAs. The formation and performance mechanisms were comprehensively investigated through a series of experiments. Importantly, this work overcomes the persistent problem of low photothermal conversion performance of PBAs, opening up new possibilities for their application in biomedicine.

Data Sharing Statement

The authors declare that the main data supporting the findings and conclusions of this study are available within the article. Extra data are available from the corresponding author upon request.

Acknowledgments

This work was financially supported by the Natural Science Foundation of Jiangsu Province of China (BK20231171) Science and Technology Innovation Project of Xuzhou City (KC22120) and Jiangsu Province Traditional Chinese medicine science and technology development program (grant No. MS2022066).

Author Contributions

All authors made a significant contribution to the work reported, whether that is in the conception, study design, execution, acquisition of data, analysis and interpretation, or in all these areas; took part in drafting, revising or critically reviewing the article; gave final approval of the version to be published; have agreed on the journal to which the article has been submitted; and agree to be accountable for all aspects of the work.

Disclosure

The authors declare that they have no known competing financial interests or personal relationships that could have appeared to influence the work reported in this paper.

References

1. Cheng L, Wang C, Feng LZ, Yang K, Liu Z. Functional nanomaterials for phototherapies of cancer. *Chem Rev*. 2014;114(21):10869–10939. doi:10.1021/cr400532z
2. Tang ZM, Liu YY, He MY, Bu WB. Chemodynamic therapy: tumour microenvironment-mediated Fenton and Fenton-like reactions. *Angew Chem Int Ed*. 2018;58:946–956. doi:10.1002/anie.201805664
3. Vankayala R, Hwang KC. Near-infrared-light-activatable nanomaterial-mediated phototheranostic nanomedicines: an emerging paradigm for cancer treatment. *Adv Mater*. 2018;30(23):1706320. doi:10.1002/adma.201706320
4. Gai SL, Yang GX, Yang PP, et al. Recent advances in functional nanomaterials for light–triggered cancer therapy. *Nano Today*. 2018;19:146–187. doi:10.1016/j.nantod.2018.02.010
5. Zhong XY, Wang XW, Li JX, Hu J, Cheng L, Yang XL. ROS-based dynamic therapy synergy with modulating tumor cell-microenvironment mediated by inorganic nanomedicine. *Coordin Chem Rev*. 2021;437:213828. doi:10.1016/j.ccr.2021.213828

6. Qi JJ, Jiang GY, Wan YQ, Liu JH, Pi FW. Nanomaterials-modulated Fenton reactions: strategies, chemodynamic therapy and future trends. *Chem Eng J*. 2023;466:142960. doi:10.1016/j.cej.2023.142960
7. Yang K, Zhang ZH, Du J, Li W, Pei ZC. Host-guest interaction based supramolecular photodynamic therapy systems: a promising candidate in the battle against cancer. *Chem Commun*. 2020;56:5865–5874. doi:10.1039/d0cc02001j
8. Li HN, Gong QY, Luo K. Biomarker-driven molecular imaging probes in radiotherapy. *Theranostics*. 2024;14(10):4127–4146. doi:10.7150/thno.97768
9. Li YK, Wu YH, Fang ZX, et al. Dendritic nanomedicine with boronate bonds for augmented chemo-immunotherapy via synergistic modulation of tumor immune microenvironment. *Adv Mater*. 2024;36(2):e2307263. doi:10.1002/adma.202307263
10. Li ZL, Zhang QF, ZQ L, et al. Branched glycopolymer prodrug-derived nanoassembly combined with a STING agonist activates an immuno-supportive status to boost anti-PD-L1 antibody therapy. *Acta Pharm Sin B*. 2024;14(5):2194–2209. doi:10.1016/j.apsb.2024.02.006
11. Liu YJ, Bhattarai P, Dai ZF, Chen XY. Photothermal therapy and photoacoustic imaging via nanotheranostics in fighting cancer. *Chem Soc Rev*. 2019;48(7):2053–2108. doi:10.1039/c8cs00618k
12. Chen JQ, Ning CY, Zhou ZN, et al. Nanomaterials as photothermal therapeutic agents. *Prog Mater Sci*. 2019;99:1–26. doi:10.1016/j.pmatsci.2018.07.005
13. Li YB, Yang J, Sun XL. Reactive oxygen species-based nanomaterials for cancer therapy. *Front Chem*. 2021;9:650587. doi:10.3389/fchem.2021.650587
14. Di XJ, Pei ZC, Pei YX, James TD. Tumor microenvironment-oriented MOFs for chemodynamic therapy. *Coord Chem Rev*. 2023;484:215098. doi:10.1016/j.ccr.2023.215098
15. Dong JL, Yu YY, Pei YX, Pei ZC. pH-responsive aminotriazole doped metal organic frameworks nanoplatform enables self-boosting reactive oxygen species generation through regulating the activity of catalase for targeted chemo/chemodynamic combination therapy. *J Colloid Interf Sci*. 2022;607:1651–1660. doi:10.1016/j.jcis.2021.09.043
16. Cao CY, Wang XR, Yang N, Song XJ, Dong XC. Recent advances of cancer chemodynamic therapy based on Fenton/Fenton-like chemistry. *Chem Sci*. 2022;13(4):863–889. doi:10.1039/d1sc05482a
17. Jin WJ, Chen ZL, Wang Y, et al. Nano metal-photosensitizer based on Aza-BODIPY-Cu complex for CDT-enhanced dual phototherapy. *Chinese Chem Lett*. 2024;35(7):109328. doi:10.1016/j.cclet.2023.109328
18. Wang XW, Zhong XY, Liu Z, Cheng L. Recent progress of chemodynamic-therapy induced combination cancer therapy. *Nano Today*. 2020;35(1):100946. doi:10.1016/j.nantod.2020.100946
19. He XJ, Lv Y, Lin YL, et al. Platinum nanoparticles regulated V2C MXene nanoplatforms with NIR-II enhanced nanozyme effect for photothermal and chemodynamic anti-infective therapy. *Adv Mater*. 2024;36(25):e2400366. doi:10.1002/adma.202400366
20. Xiong PZ, Wei XD, Zhou L, et al. Near-infrared light-triggered MXene nanocomposite for tumor-specific mild photothermal-enhanced chemodynamic therapy. *Adv Funct Mater*. 2024;2405124. doi:10.1002/adfm.202405124
21. Hu TT, Yan L, Wang ZD, et al. A pH-responsive ultrathin Cu-based nanoplatform for specific photothermal and chemodynamic synergistic therapy. *Chem Sci*. 2021;12(7):2594–2603. doi:10.1039/d0sc06742c
22. Peng H, Ren GP, Hampp N, Wu AG, Yang F. The development of rare-earth combined Fe-based magnetic nanocomposites for use in biological theranostics. *Nanoscale*. 2023;15(25):10513–10528. doi:10.1039/d3nr01373a
23. Xiong ZJ, Sun LL, Yang H, et al. Ni-alginate hydrogel microspheres with sustained interleukin 2 release to boost cytokine-based cancer immunotherapy. *Adv Funct Mater*. 2023;33(7):2211423. doi:10.1002/adfm.202211423
24. Cai DP, Liu B, Wang DD, et al. Rational synthesis of metal–organic framework composites, hollow structures and their derived porous mixed metal oxide hollow structures. *J Mater Chem A*. 2016;4(1):183–192. doi:10.1039/c5ta07085f
25. Shokouhimehr M, Soehnlen ES, Khitrin A, Basu S, Huang SD. Biocompatible Prussian blue nanoparticles: preparation, stability, cytotoxicity, and potential use as an MRI contrast agent. *Inorg Chem Commun*. 2010;13(1):58–61. doi:10.1016/j.inoche.2009.10.015
26. Du L, Du CY, Chen GY, Kong FP, Yin GP, Wang Y. Metal–organic coordination networks: Prussian blue and its synergy with Pt nanoparticles to enhance oxygen reduction kinetics. *ACS Appl Mater Interfaces*. 2016;8(24):15250–15257. doi:10.1021/acsami.6b02630
27. Wang Y, Wang YZ, Gao HW, Huang ZH, Hao QL, Liu B. Interface-induced contraction of core-shell Prussian blue analogues toward hollow Ni-Co-Fe phosphide nanoboxes for efficient oxygen evolution electrocatalysis. *Chem Eng J*. 2023;451:138515–138523. doi:10.1016/j.cej.2022.138515
28. Xu MJ, Zhang Q, Zhu ZQ, Xue YW, Zhang T, Hong JM. Chemical etching to regulation oxygen vacancies on Mn-Fe PBA for highly efficient degradation of bisphenol A and Acetaminophen. *J Clean Prod*. 2022;377:134258–134270. doi:10.1016/j.jclepro.2022.134258
29. Zeng YX, Xu JZ, Wang Y, Li S, Luan DY, Lou XW. Formation of CuMn Prussian blue analog double-shelled nanoboxes toward long-life Zn-ion batteries. *Angew Chem Int Ed*. 2022;61(48):202212031–202212037. doi:10.1002/anie.202212031
30. Mukherjee S, Rao BR, Sreedhar B, Paik P, Patra CR. Copper Prussian blue analogue: investigation into multifunctional activities for biomedical applications. *Chem Commun*. 2015;51(34):7325–7328. doi:10.1039/c5cc00362h
31. Han L, Yu XY, Lou XW. Formation of Prussian-blue-analog nanocages via a direct etching method and their conversion into Ni–Co-Mixed oxide for enhanced oxygen evolution. *Adv Mater*. 2016;28(23):4601–4605. doi:10.1002/adma.201506315
32. Li WJ, Han C, Cheng G, Chou SL, Liu HK, Dou SX. Chemical properties, structural properties, and energy storage applications of Prussian blue analogues. *Small*. 2019;15(32):1900470–1900490. doi:10.1002/smll.201900470
33. Ojha RP, Pal S, Prakash R. Cu-Fe Prussian blue analog nanocube with intrinsic oxidase mimetic behaviour for the non-invasive colorimetric detection of isoniazid in human urine. *Microchem J*. 2021;171:106854–106862. doi:10.1016/j.microc.2021.106854
34. Ishizaki M, Ohshida E, Tanno H, et al. H_2O_2-sensing abilities of mixed-metal (Fe-Ni) Prussian blue analogs in a wide pH range. *Inorg Chim Acta*. 2020;502:119314–119319. doi:10.1016/j.ica.2019.119314
35. Jia QJ, Su FF, Li ZZ, et al. Tunable hollow bimetallic MnFe Prussian blue analogue as the targeted pH-responsive delivery system for anticancer drugs. *ACS Appl Biomater*. 2019;2(5):2143–2154. doi:10.1021/acsabm.9b00129
36. Jia QJ, Li ZZ, Guo CP, et al. PEGMA-modified bimetallic NiCo Prussian blue analogue doped with Tb(III) ions: efficiently pH-responsive and controlled release system for anticancer drug. *Chem Eng J*. 2020;389:124468–124479. doi:10.1016/j.cej.2020.124468
37. Li ZH, Chen Y, Sun YX, Zhang XZ. Platinum-doped Prussian blue nanozymes for multiwavelength bioimaging guided photothermal therapy of tumor and anti-inflammation. *ACS Nano*. 2021;15(3):5189–5200. doi:10.1021/acsnano.0c10388

38. Li J, Liu XM, Tan L, et al. Zinc-doped Prussian blue enhances photothermal clearance of staphylococcus aureus and promotes tissue repair in infected wounds. *Nat Commun*. 2019;10(1):4490. doi:10.1038/s41467-019-12429-6
39. Zhu BC, Tan HY, Fan JY, Cheng B, Yu JG, Ho WK. Tuning the strength of built-in electric field in 2D/2D g-C_3N_4/SnS_2 and g-C_3N_4/ZrS_2 S-scheme heterojunctions by nonmetal doping. *J Materiomics*. 2021;7(5):988–997. doi:10.1016/j.jmat.2021.02.015
40. Su K, Tan L, Liu XM, et al. Rapid photo-sonotherapy for clinical treatment of bacterial infected bone implants by creating oxygen deficiency using sulfur doping. *ACS Nano*. 2020;14(2):2077–2089. doi:10.1021/acsnano.9b08686
41. Du M, Geng PB, Pei CX, et al. High-entropy Prussian blue analogues and their oxide family as sulfur hosts for lithium-sulfur batteries. *Angew Chem Int Ed*. 2022;61(41):202209350–202209359. doi:10.1002/anie.202209350
42. Wang M, Huang Q, Ma RX, et al. Construction of Mn doped Cu_7S_4 nanozymes for synergistic tumor therapy in NIR-I/II bio-windows. *Colloids Surface B*. 2024;234:113689. doi:10.1016/j.colsurfb.2023.113689
43. Qin YH, Gu WJ, Wu YP, Huang QL, Zhang M. Synthesis of Prussian blue analogue nanoboxes with enhanced photothermal and catalytic performance. *J Photochem Photobiol A*. 2024;454:115694. doi:10.1016/j.jphotochem.2024.115694
44. Hao YT, Mao LZ, Zhang RJ, Liao XS, Yuan MM, Liao WZ. Multifunctional biodegradable Prussian blue analogue for synergetic photothermal/photodynamic/chemodynamic therapy and intrinsic tumor metastasis inhibition. *ACS Appl Bio Mater*. 2021;4(9):7081–7093. doi:10.1021/acsabm.1c00694
45. Zhong DL, Wang YX, Xie F, et al. A biomineralized Prussian blue nanotherapeutic for enhanced cancer photothermal therapy. *J Mater Chem B*. 2022;10(25):4889–4896. doi:10.1039/d2tb00775d
46. He YL, Guo SW, Zhang Y, Liu Y, Ju HX. NIR-II reinforced intracellular cyclic reaction to enhance chemodynamic therapy with abundant H_2O_2 supply. *Biomaterials*. 2021;275:120962. doi:10.1016/j.biomaterials.2021.120962.
47. Li JC, Yu XR, Jiang YY, et al. Second near-infrared photothermal semiconducting polymer nanoadjuvant for enhanced cancer immunotherapy. *Adv Mater*. 2021;33(4):e2003458. doi:10.1002/adma.202003458
48. Ding YN, Liu H, Gao LN, et al. Fe doped Ag_2S with excellent peroxidase-like activity for colorimetric determination of H_2O_2. *J Alloys Compd*. 2019;785:1189–1197. doi:10.1016/j.jallcom.2019.01.225
49. Zhang Y, Zhou ZF, Wen FF, et al. A flower-like MoS_2-decorated $MgFe_2O_4$ nanocomposite: mimicking peroxidase and colorimetric detection of H_2O_2 and glucose. *Sensor Actuat B-Chem*. 2018;275:155–162. doi:10.1016/j.snb.2018.08.051
50. Yu XY, Yu L, Wu HB, Lou XW. Formation of nickel sulfide nanoframes from metal–organic frameworks with enhanced pseudocapacitive and electrocatalytic properties. *Angew Chem Int Ed*. 2015;54:5331–5335. doi:10.1002/anie.201500267
51. Yang YC, Tian Q, Wu SQ, et al. Blue light-triggered Fe^{2+}-release from monodispersed ferrihydrite nanoparticles for cancer iron therapy. *Biomaterials*. 2021;271:120739. doi:10.1016/j.biomaterials.2021.120739
52. Emamgholizadeh Minaei S, Khoei S, Khoee S, Karimi MR. Tri-block copolymer nanoparticles modified with folic acid for temozolomide delivery in glioblastoma. *Int J Biochem Cell B*. 2019;108:72–83. doi:10.1016/j.biocel.2019.01.010